Spinodal decomposition in lead-free piezoelectric BaTiO3–CaTiO3–BaZrO3 crystals

Gabriel Buse, Cong Xin, Pascal Marchet, Ana Borta-Boyon, Maï Pham-Thi, Hughes Cabane, Emmanuel Véron, Michaël Josse, Matias Velázquez, Michel Lahaye, et al.

Spinodal decomposition in lead-free piezoelectric $BaTiO_3$-$CaTiO_3$-$BaZrO_3$ crystals

Gabriel Buse[1,2], Cong Xin[1,2,3], Pascal Marchet[4], Ana Borta-Boyon[5], Mai Pham-Thi[5], Hughes Cabane[6], Emmanuel Veron[7], Michael Josse[1,2], Matias Velazquez[1,2], Michel Lahaye[8], Eric Lebraud[1,2], Mario Maglione[1,2], Philippe Veber [1,2,9,]*

[1] CNRS, ICMCB, UMR 5026, Pessac F-33600, France

[2] Université de Bordeaux, ICMCB, UMR 5026, Pessac F-33600, France

[3] Materials, Research and Technology Department, Luxembourg Institute of Science and Technology-University of Luxembourg, 41 Rue du Brill, 4422 Belvaux, Luxembourg

[4] Université de Limoges, IRCER, UMR 7315, Limoges F-87068, France

[5] Thales Research and Technology, 1, av. Fresnel, Campus de l'Ecole Polytechnique – 91767 PALAISEAU Cedex, France

[6] CristalInnov, Cleanspace , Parc d'Activités Alpespace, 354 voie Magellan, F-73800 Sainte Hélène du Lac, France

[7] Conditions Extrêmes et Matériaux : Haute Température et Irradiation, Site Haute Température, CS 90055, 1D avenue de la Recherche Scientifique, 45071 Orléans cedex 2, France

[8] Placamat, UMS 3626, CNRS, Université de Bordeaux, 87 avenue Albert Schweitzer, 33600 Pessac, France

[9] Université Lyon, Université Claude Bernard Lyon 1, CNRS, Institut Lumière Matière UMR 5306, F-69100, Villeurbanne, France

KEY WORDS: Lead-free / Piezoelectrics / Top Seeded Solution Growth / Spinodal decomposition

ABSTRACT: Polycrystals and centimeter-sized $BaTiO_3$-based single crystals were grown by top seeded solution growth from the $BaTiO_3$-$CaTiO_3$-$BaZrO_3$ system. High effective partition coefficients of Zr ranging from 15 to 6 with small Zr content have been calculated from Castaing micro-probe measurements whereas those of Ca increase slightly from 0.45 to 0.7. A spinodal decomposition mechanism is emphasized during the growth leading to the emergence of two phases with close compositions. Chemical analysis displayed periodical Zr and Ca contents fluctuations within the whole boules and Rietveld measurements highlighted two phases belonging to perovskite structures with tetragonal P4mm and orthorhombic Amm2 space groups. Samples with various calcium and zirconium contents were characterized by means of dielectric and piezoelectric measurements. Most efficient samples are indistinctly polycrystals or oriented single crystals where electromechanical performances are compositional-dependent. Polycrystalline samples and single crystals oriented along $(001)_{pc}$ and $(110)_{pc}$ displayed Curie temperatures ranging from 50°C to 111°C. Electromechanical coupling factor up to 58% and piezoelectric charge coefficient d_{33}=496 $pC.N^{-1}$ were obtained at room temperature. The miscibility gap between the two perovskite solid solutions as well as Ca and Zr elements content variation in single

crystals lower crystal piezoelectric response which remains nonetheless of the same efficiency compared to that of ceramics of the same composition.

1. Introduction

Due to the environmental toxicity of lead, lead-free piezoelectric materials attract more and more attention. Lead-based ferroelectric materials such as lead zirconate titanate $PbZr_{1-x}Ti_xO_3$ (PZT) [1,2] are the most widely used piezoelectrics, because of their excellent properties. In last years, the environmental and health hazards of lead have been recognized, leading to an increased interest in the development of lead-free piezoelectric materials[3–7]. The main challenge is to find materials with equal or even higher piezoelectric response than the lead-based materials.

While lead-free piezoelectric ceramics exhibit lower performance than PZT, among the three main families of promising lead-free piezoelectrics[3,6,8,9] recent reports have shown outstanding piezoelectric constants up to 620 $pC{\cdot}N^{-1}$ in $(1-x)BaTi_{0.8}Zr_{0.2}O_3$-$xBa_{0.7}Ca_{0.3}TiO_3$ (BCTZ) solid solution [5,6,10,11]. BCTZ solid solution properties make this system promising as alternative to lead-containing materials. Furthermore, single crystals should display better electromechanical properties than ceramics so that it is expected that BCTZ single crystals would exhibit piezoelectric constants of about 1500-2000 $pC{\cdot}N^{-1}$ as predicted by Liu *et al.* [10]. Recently, we reported [12,13] early growth attempt of BCTZ single crystals in $BaTiO_3$-$CaTiO_3$-$BaZrO_3$ pseudo-ternary solid-solution with various zirconium (Zr) and calcium (Ca) contents where a continuous evolution of their electrical properties from relaxor to pure ferroelectric behavior was highlighted with Ca and Zr contents.

In the present paper, we focus on single crystal growth by Top-Seeded Solution Growth method of BCTZ following the methodology reported in literature[13] where various compositions were obtained in order to reach enhanced piezoelectric properties. Centimeter-sized polycrystalline

boules and single crystals with varying compositions were obtained. DSC and high temperature XRD analysis as well as chemical mapping performed by Castaing Electron Probe Microscopy Analysis (EPMA) are presented. Effective segregation of elements and periodical oscillations of their contents are discussed with respect to the growth direction. The correlation between chemical contents and Rietveld XRD analysis is undertaken and a spinodal decomposition in the BCTZ system is highlighted. Large-sized boules allowed to extract oriented centimeter-sized single crystal samples. Finally, dielectric measurements are presented and highlight the broadening of the tetragonal to orthorhombic phase transition featuring the spinodal decomposition. Piezoelectric measurements on some as-grown and annealed polycrystals and single crystals are displayed. The results are discussed with respect to data of literature about ceramics samples over a wide range of compositions.

2. Experimental procedure

2.1 Chemical and physical analysis

Castaing Electron Probe Microscopy Analysis (EPMA) were performed with a CAMECA SX-100 apparatus with a wavelength dispersive spectrometer working at 15 kV. Reference samples for quantitative analysis of elements [13] were chosen in order to reach an experimental accuracy of $\Delta\%Zr=\Delta\%Ca=\pm 0.3$mol.% per analysis point in the investigated concentrations range.

Dielectric and piezoelectric measurements were performed by electroding the major faces of crystals using gold sputtering and silver wires attached to these electrodes with silver paste. The samples were set in a homemade cell enabling the temperature to be scanned from -160°C up to 227°C. Prior to such low temperature run, the cell was pumped down and a slight underpressure

of dry Helium ($P=10^{-1}$mPa) was introduced so as to avoid moisture adsorption. The samples were electrically connected to the output port of a HP4194 impedance analyzer with an operating frequency range of 100Hz–10MHz. Samples were poled under a DC electric field by the increasing field method up to 1 $kV.cm^{-1}$ at room temperature. The dielectric and piezoelectric properties were recorded during poling with un impedance analyzer (4294A Agilent). The temperature dependence of dielectric constant and dielectric losses were characterized using an environmental chamber Pyrox. The d_{33} values of the poled samples were measured by Berlincourt method with a Pennebaker Piezo d_{33} meter (Model 8000). The piezoelectric constant along with corresponding electromechanical coupling coefficient for the length thickness mode were determined at different temperatures on the basis of IEEE standards [6].

Differential scanning calorimetry (Netzsch STA 449) was performed between room temperature and 1350°C in platinum crucibles under air atmosphere. Both heating and cooling signals were recorded using $10°C.mn^{-1}$ rate. DSC signal was corrected from baseline obtained for empty crucibles.

In situ High temperature X-ray diffraction measurements were performed on a Bruker D8 Advance Bragg-Brentano (CuKα1,2 radiation) diffractometer equipped with a linear Vantec detector. Powders were placed on a platinum ribbon in an HTK16 Anton Paar chamber. The temperature behavior of this ribbon was previously calibrated using the known phase transitions and thermal expansion of a corundum reference. Diffractograms were collected between 15 and 70° (2θ) with a 0.024° step size. The samples were heated from 1150°C to 1450°C at a rate of $10°C.min^{-1}$, and the ramp was stopped for each diffractogram every 25°C to avoid any change during the data collection.

X-ray diffraction (XRD) patterns were collected on a Bragg-Brentano θ-2θ geometry diffractometer (PANalitycal X'pert MPD-PRO, Cu $K\alpha_1$, $\lambda = 0.15056$ nm), equipped with a primary germanium monochromator, a sample spinner and a planar detector (X'celerator). The data were collected over an angular range of $2\theta = 10°$-$130°$ and each acquisition lasted for 25 hours. The powders were ground and sifted with a 40 microns sieve for a better homogeneity of the particles size. The samples were carefully prepared on stainless steel sample holder using a razor blade to prevent preferential orientations. XRD patterns were studied by Rietveld refinements (Jana 2006 software[15]) using the known space groups of $BaTiO_3$[16]. Using a conventional notation for perovskite compounds, the pseudo-cubic Miller indices will be hereafter written using "pc" indices.

Laue back-scattering patterns were recorded using a CCD-camera device (Photonic Science dual lens coupled X-rays Laue system) after a 3–5 min stationary crystal irradiation with polychromatic X-rays supplied by a molybdenum anticathode. Single crystals were cut along pseudo-cubic (pc) directions with a diamond wire saw with an absolute accuracy less than 1°.

The grains morphology of the polycrystalline samples was observed with an optical microscope Zeiss Axio Scope.

2.2 Synthesis and crystal growth

Synthesis of initial loads were prepared from $BaCO_3$, $CaCO_3$, TiO_2, ZrO_2 raw powders with 99.99%-purity from Fox Chemicals GmbH. Based on previous works [12,13], growth attempts were carried out with a self-flux composed of an excess of BaO and TiO_2. Initial load compositions (Table 1) are considered as a global solid solution including the solvent and the solute to be grown, so that 100% of Ba and Ca cations are in A site and 100% of Ti and Zr cations

	Solution composition (mol.%)				As-grown boule		
No. Attempt	**Ba**	**Ca**	**Ti**	**Zr**	**40X40mm crucible**	**80X80mm crucible**	**Reference**
1st attempt - BCTZ1	85.0%	15.0%	90.0%	10.0%	Polycrystal	X	[12,13]
2nd attempt - BCTZ2	77.0%	23.0%	98.0%	2.0%	Polycrystal	X	[12,13]
3rd attempt - BCTZ3	76.5%	23.5%	97.6%	2.4%	mm-sized single crystal	X	[12,13]
4th attempt - BCTZ4	76.8%	23.2%	97.8%	2.2%	mm-sized single crystal	X	This work
5th attempt - BCTZ5	77.3%	22.7%	97,9%	2,1%	mm-sized single crystal	mm-sized single crystal	This work
6th attempt - BCTZ6	88,7%	11,3%	98,7%	1,3%	mm-sized single crystal	cm-sized single crystal	This work
7th attempt - BCTZ7	92,5%	7,5%	98,7%	1,3%	cm-sized single crystal	X	This work

Table 1. Normalized compositions of initial liquid solutions for BCTZ for growth and resulting obtained crystals.

The solid state reaction was performed by thermal treatment as described by Benabdallah *et al.*[12] in a platinum crucible under air atmosphere. Single crystals were grown in 40X40mm or 80X80mm iridium crucibles by using the Top-Seeded Solution Growth technique (TSSG). Cyberstar Oxypuller™ induction furnaces working under controlled argon atmosphere were used. The growing crystal weight was monitored continuously during the whole process. Longitudinal and transversal temperature gradients were estimated to be around 50°C.cm^{-1}. Growth attempts were performed manually in a 40X40mm crucible and with automatic crystal shape control software designed by Cyberstar in a 80X80mm crucible. After synthesis and growth, no defined compounds nor secondary parasitic phases have been obtained in the temperature range where the growth took place.

First growth attempts were performed on both (001)-oriented $BaTiO_3$ and $SrTiO_3$ seeds with BCTZ4 and BCTZ6 compositions respectively (Figure 1a and 1b). Because the 1st order hexagonal-cubic phase transition of $BaTiO_3$ at T≈1460°C [17] occurs in the growth temperature range, the boule featured cracks and mm-sized grains as well as large polycrystalline zones without defects. In addition, we noted that creeping of the solution all along the seed during the growth has been detrimental to control the seeding and thus the boule quality. During the growth along (001)-

oriented $SrTiO_3$ seed, which does not exhibit any phase transition in the BCTZ growth temperature range, the growth was out of control. We observed both the continuous decrease of $SrTiO_3$ seed's weight dissolving in the Sr-free BCTZ4 solution and, simultaneously, the crystallization of a BCTZ ring around the seed in the solution which was assumed to be supersaturated with other elements than Sr. Indeed, $SrTiO_3$-$BaTiO_3$ and $SrTiO_3$-$CaTiO_3$ systems[18,19] exhibit large solid solutions where the solubility of $SrTiO_3$ is allowed in both $BaTiO_3$ and $CaTiO_3$. Since the considered initial liquid BCTZ6 solution is mainly composed of Ba (88.7 mol.%) titanate and Ca (11.3 mol.%) titanate with a global Ti content of 98.7 mol.% (see Table 1), the phase diagrams confirm that $SrTiO_3$ dissolved in Sr-free BCTZ6 solution.

Despite a high temperature orthorhombic-tetragonal phase transition[20], $CaTiO_3$ may have been considered as a suitable seed for BCTZ growth because crackless $CaTiO_3$ can be grown directly from its liquid phase [21,22]. However, due to the unavailability of other kind of perovskite-related compounds with same elements containing either Ba, Ca, Ti or Zr elements, a 3-mm-thick iridium wire was finally used in order to initiate the nucleation and crystal growth. The rod was dipped into the melt after homogenization of the liquid solution for 24h. A rotation speed ranging from 0.5 to 30 rpm and pulling velocity varying from 0.01 to 1.5 $mm.h^{-1}$ were investigated. The growth was driven by decreasing the temperature at a rate ranging in between $0.5°C.h^{-1}$ and $1,5°C.h^{-1}$. At the end of the growth process, the boules were set 5 mm above the liquid surface in order to reduce the thermal stress and cooled down to room temperature in 72 h.

3. Results and discussion

3.1 Crystal growth

Crystal growth attempts exhibited saturation temperatures ranging from 1485 to 1570 °C indicating that the saturation temperature is mainly a function of Ca and Zr contents in the crystals. Owing to the narrow investigated ranges of Zr and Ca concentrations, crystal shape and habits in the following are assumed to be related only to the growth parameters.

On the one hand, crystal growth with BCTZ4 to BCTZ6 (Figure 1c to 1f) compositions performed in a 40x40mm iridium crucible with manual crystal geometry control led to polycrystalline centimeter-sized BCTZ boules with rough cylindrical shape (Figure 1c and 1d). Boules exhibit mm-sized grains when using a pulling rate above 0.05 $mm.h^{-1}$, a cooling rate above 1.5 $°C.h^{-1}$ and a rotation speed about 30 rpm. Crystal growth with BCTZ7 composition performed below these values with low rotation speed about 6-8 rpm resulted in facetted boules (Figure 1f) with centimeter-sized single crystals at the bottom of the boule. Most of the boules are delimited by radial cracks around the Ir rod (Figure 1c) and they frequently exhibit a foot shape adjacent to a concave interface at the bottom. In some case, manually as-grown boules exhibit an apparent 6-fold axis-like faceting at the top of the BCTZ6 boule (Figure 1e).

Figure 1. Growth into a 40X40mm iridium crucible with manual shape control: (a) BCTZ4 boule grown onto a $BaTiO_3$ seed. Insert: Optical microscopy micrograph with the individual component crystallites and grain boundaries; (b) BCTZ6 growth attempt onto a $SrTiO_3$ seed; (c) BCTZ5 boule; (d) BCTZ6 boule; (e) Top facetting around a 6-fold axis-like in BCTZ6 as-grown crystals; (f) BCTZ7 boule. Insert: Laue pattern of single crystal extracted from the bottom of the boule.

However, unlike it is observed for $BaTiO_3$ [17,23] and $(Ba,Ca)TiO_3$ solid solution, no 1st order cubic-hexagonal high-temperature phase transition [24], which may cause severe cracks, was detected up to the saturation temperature as showed by DSC analysis up to 1300 °C (Figure 2) and HT XRD up to 1450°C (Figure 3).

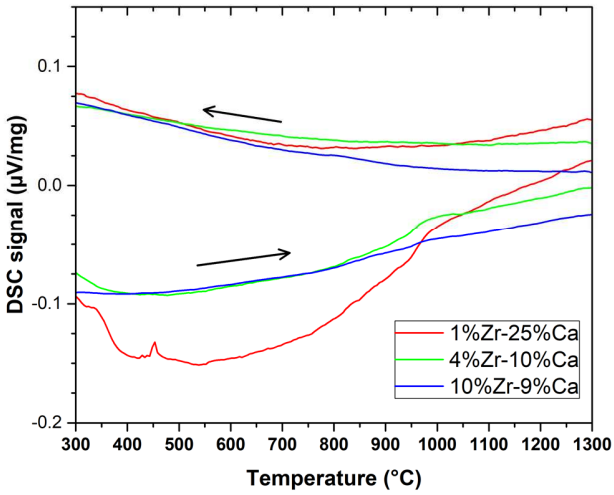

Figure 2. Differential Scanning Calorimetry patterns of three BCTZ samples with various composition. No sign of high temperature phase transition is detected up to 1300°C. Peak observed on the red curve around 460°C is attributed to an experimental artefact.

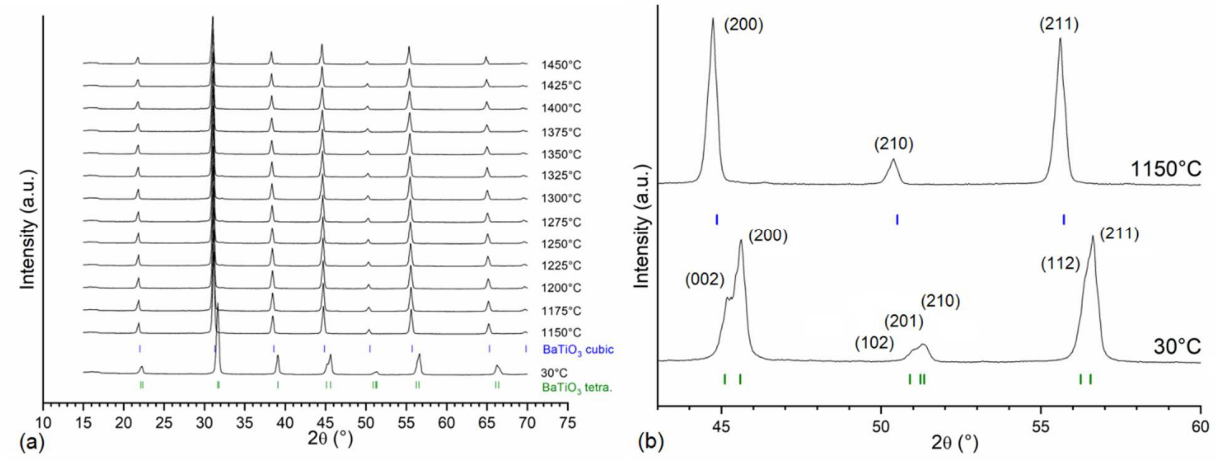

Figure 3. (a) High temperature XRD pattern of a BCTZ polycrystal sample containing 1%Zr and 25%Ca. Except thermal expansion and transition from tetragonal (diffractogram at 30°C) to cubic structure (diffractogram at 1150°C) , no additional phase transition is detected up to 1450°C. (b)

Zoom on typical (hkl) peaks showing the transition from tetragonal (green) to cubic (blue) structure.

Hence, assuming that no high temperature phase transition occurs in BCTZ because modified-$BaTiO_3$ should exhibit lower cubic-hexagonal transition temperature than that of pure $BaTiO_3$ [17], such cracks are assumed to be caused during the cooling by the different thermal expansion coefficients between Ir and BCTZ[25,26]. Apparent faceting is attributed to crystal habit in the thermal configuration of the furnace. On the other hand, crystal growth with BCTZ5 composition performed in 80X80mm Ir crucible with automatic boule shape control software displayed single crystal with a spiral shape (Figure 4a).

As previously referenced for the Czochralski growth of similar perovskite such as $DyScO_3$ [27] and $SrTiO_3$ [28], foot or spiral formation in BCTZ occurred because the heat transport via the crystal is hindered by low thermal conductivity as well as by the plausible low infrared transparency induced by the reduction of Ti(+IV) into Ti(+III) and the decreasing of band gap energy with temperature Automatic crystal geometry control generates particularly spiral shaped boules because of the continuous mass regulation which occurs at the crystal foot tip during the crystal growth process. Finally, in order to avoid foot or spiral growth and to reduce as much as possible cracks, a growth attempt with BCTZ6 composition on a 2 mm-thick iridium rod has been performed at 0.5 rpm and 1.5 $mm.h^{-1}$. This led to a single crystal with cylindrical shape about 50 mm wide and weighing 330 g. Centimeter-sized oriented single crystals were successfully extracted from the boule (Figure 4b).

Figure 4. Growth into a 80X80mm iridium crucible with automatic crystal geometry control: (a) Spiral as-grown boule obtained on a 2mm-thick iridium wire and pulled from BCTZ5 composition (b) 330-g crystal grown from BCTZ6 composition with 50mm diameter. Insert: $(001)_{pc}$ oriented centimeter-sized single crystal with $(Ba_{0.905}Ca_{0.095})(Ti_{0.943}Zr_{0.057})$ average composition.

3.2. Chemical analysis

EPMA quantitative analysis allowed to calculate Zr and Ca effective partition coefficients k_{eff} [29] (Figure 5) where the partition coefficient k_{eff} is defined as the molar ratio in between the content of a considered element at the early beginning of the crystal and its initial content in liquid solution.

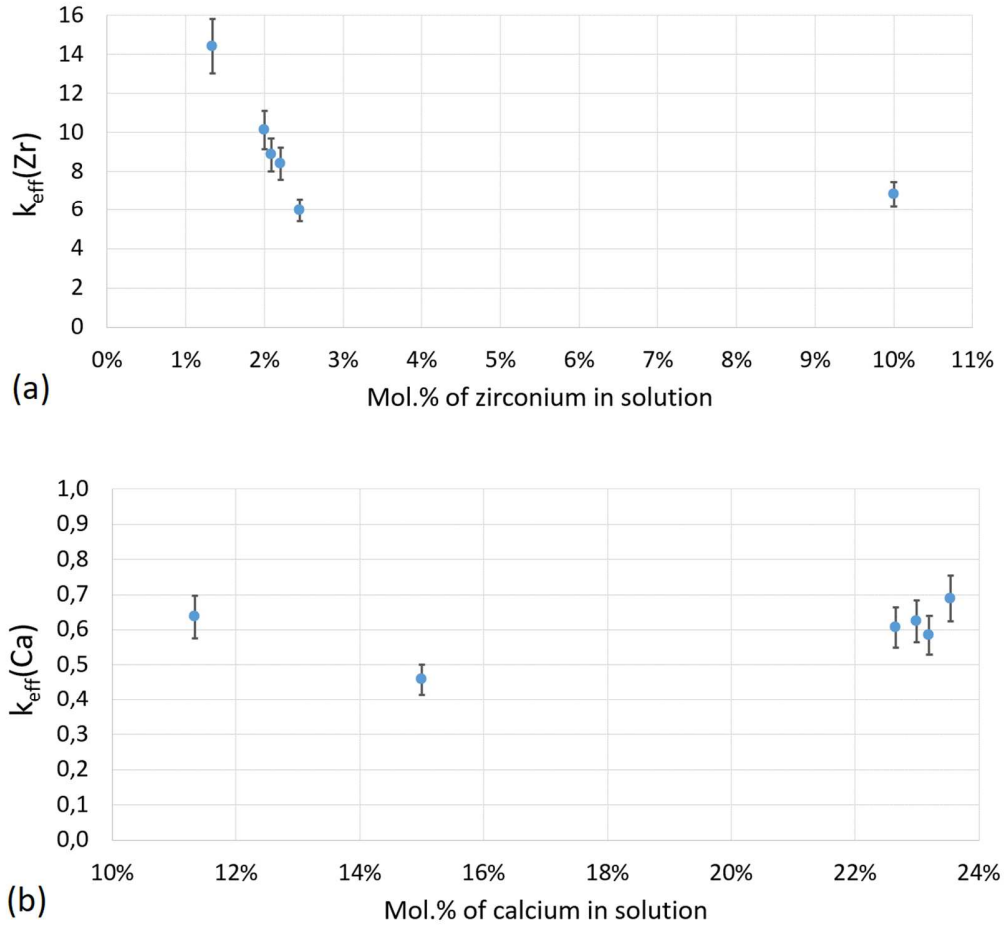

Figure 5. Effective partition coefficient of (a) Zr and (b) Ca as a function of their molar content in liquid solution.

Effective partition coefficient of Zr is significantly greater than 1 contrary to that of Ca which remains lower than 1. Consequently, as depicted on Figure 6, a strong decreasing of Zr content and an increasing of Ca content with respect to the radius and the length of boule is measured.

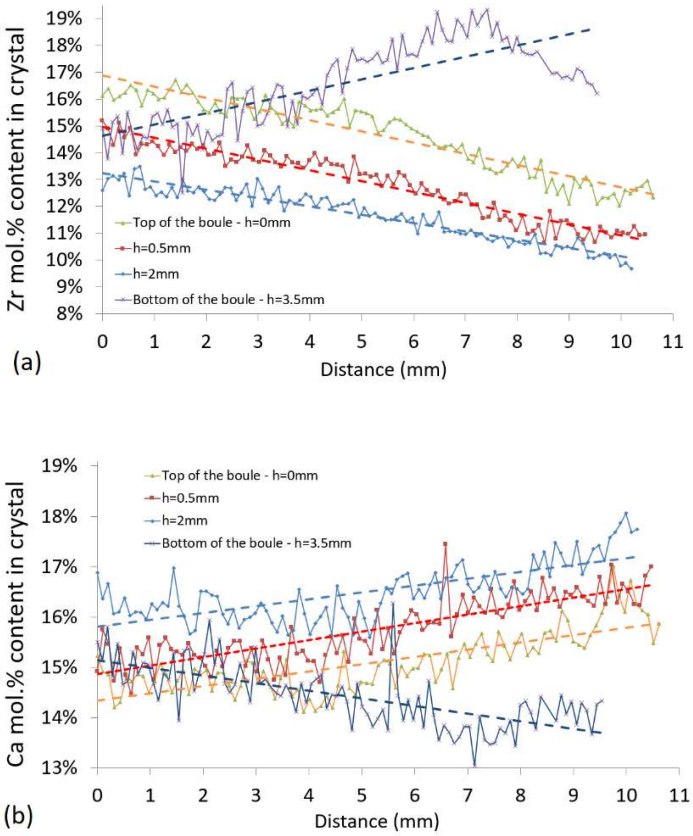

Figure 6. Transversal evolution of (a) Zr and (b) Ca contents in as-grown BCTZ4 boule for 4 different altitudes h in the crystal depicted in figure 1a. The radial distance 0mm corresponds to the center of the boule.

However, analysis show a reverse tendency at the end of the boules. Zr and Ca contents respectively increase and decrease with the length and radius. This is meaningful of the change of the interface shape which become concave at the end of growth as it is observed on crystals of Figure 1a and Figure 1f. At the end of the growth, crystallization occurs from the periphery to the core of the boule. This feature confirms that the release of the heat of crystallization is particularly hindered at the core of the boule, inducing thus a change of the interface shape, then, the emergence of a growth foot on the side of the boule. In addition, chemical analysis systematically reveals

periodical fluctuations of the Zr content and, to a lower extent, of Ca content with amplitudes well beyond the accuracy limit (e.g. 0.3 mol.%) of the analysis (Figure 7).

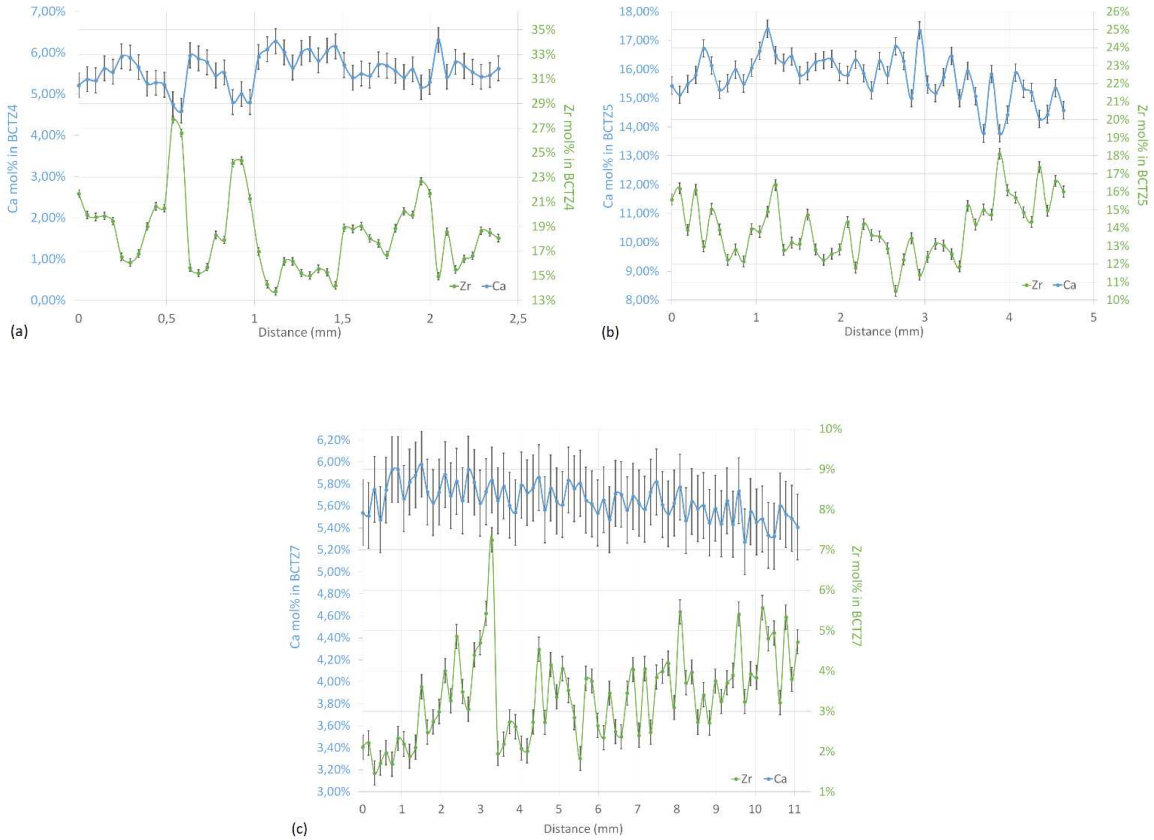

Figure 7. Molar fluctuations of Ca and Zr contents measured by EPMA analysis for (a) BCTZ4, (b) BCTZ5 and (c) BCTZ7 crystals extracted randomly in as-grown boules.

It has been observed that the amplitudes of these periodical fluctuations are ranged from ±0.5 mol.% and raise up to ±5 mol.% for Zr and ±2 mol.% for Ca. The particular case of BCTZ6 single crystal is relevant of such fluctuations. BCTZ6 sample with $(Ba_{0.905}Ca_{0.095})(Ti_{0.943}Zr_{0.057})O_3$ average composition shows typical periodical Ca and Zr content fluctuations, with a wavelength about 1-1.5 mm, which evolve like waves in phase opposition (Figure 8).

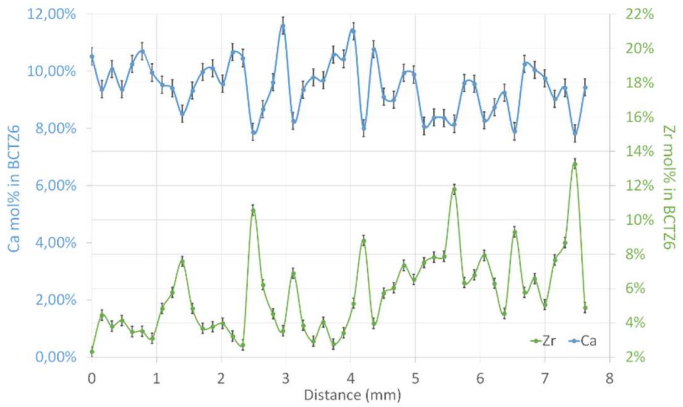

Figure 8. Molar fluctuations of Ca and Zr contents in a single crystal grown from BCTZ6 solution. Crystal with $(Ba_{0.905}Ca_{0.095})(Ti_{0.943}Zr_{0.057})$ average composition shows oscillations of Ca and Zr contents similar to phase opposition and features the presence of two solid solutions due to spinodal decomposition.

That suggests strongly the existence of two solid solutions with extreme compositions corresponding to $(Ba_{0.884}Ca_{0.116})(Ti_{0.977}Zr_{0.023})O_3$ and $(Ba_{0.922}Ca_{0.078})(Ti_{0.867}Zr_{0.133})O_3$. As already observed in $BaZrO_3$-$CaZrO_3$ [30] and $BaTiO_3$-$CaTiO_3$ [24] systems from which the BCTZ solid solution derives, a miscibility gap allows for the coexistence of two solid solutions through a phase segregation mechanism. Investigated BCTZ compositions range exhibits the same trend where two Ca- and Zr-substituted $BaTiO_3$ solid solutions are coexisting through a spinodal decomposition at high temperature. Such a phenomenon has not been observed in BCTZ ceramics of same compositions because the synthesis time and temperature (~15H and 1350°C) [31] are drastically lower to those (~ up to 2 weeks and 1570°C) of single crystal growths and prevent then the ceramics from phase separation. As the BCTZ compositional disorder implies Ca and Zr low amplitude concentrations fluctuations through the boules, the system becomes unstable at high temperature and finally decomposes. Hence, the spinodal demixion is favored by the resulting

continuous annealing of the already-as-grown crystal during the whole growth process. This out of equilibrium process leads to pseudo-periodic distribution of the precipitated phases when interrupted before end. This is similar in some respect to Ostwald ripening of precipitate particles but with uphill diffusion since the diffusion takes place against the concentration gradient.

Since BCTZ6 samples exhibit an outstanding signature of a spinodal decomposition in BCTZ system through periodical fluctuation of their Zr and Ca contents, particular endeavors on XRD and dielectric measurements performed on $(001)_{pc}$ BCTZ6 samples are presented in the following.

3.3 Rietveld analysis

XRD patterns from BCTZ6 batch were recorded on powdered samples made from crushed single crystals. Owing to the strong segregation of elements during the growth, samples have been cut in as-grown boules in order to reach a relative composition accuracy about ±1.5 mol.% for Zr and ±0.5 mol.% for Ca with average size of $5x2x0.5mm^3$. XRD patterns were obtained both on as-grown and annealed samples of same composition (Figure 9). The annealing process was carried out at 1350°C for 500h in air atmosphere.

As expected, XRD patterns evidences only perovskite phase without detection of any secondary phase. For both as-grown and annealed samples, the main peaks are splitted, indicating a non-cubic symmetry: $(00l)_{pc} \rightarrow (00l)_{tetra} + (h00)_{tetra}$ and $(110)_{pc} \rightarrow (101)_{tetra} + (110)_{tetra}$ (see arrows on Figure 9b and c). In addition, the intensities and shape of diffraction peaks was changed by annealing process.

This splitting of the main peaks could indicate a tetragonal symmetry, similar to the one of $BaTiO_3$. The position of tetragonal peaks obtained by simulation of the diagram (P4mm space group) is reported in Figure 9. The refined lattice parameters are a = 3.993(8) Å, c = 4.019(8) Å

and c/a = 1.007, thus similar to the one of tetragonal $BaTiO_3$ (a = 3.983 Å, c= 4.018 Å, c/a =1.009). However, these results clearly indicate that the splitting of the $(111)_{pc}$ peak is incompatible with the tetragonal symmetry (Figure 9c). Neither are the intensity ratio of the $(00l)_{tetra}$ / $(h00)_{tetra}$ / and $(101)_{tetra}$ / $(110)_{tetra}$ diffraction peaks. Indeed, this ratio would be around two for the P4mm space group because of multiplicity (Figure 9b and c for annealed powder). Taking into account the simultaneous splitting of the $(100)_{pc}$ and $(111)_{pc}$, we also considered the orthorhombic Amm2 structure of $BaTiO_3$ (a_{pc} √2 x a_{pc} √2 x a_{pc}) alone and R3m structure of $BaTiO_3$. Neither were the simulations successful for any single phase. (The results of these Rietveld refinements are included in supplementary materials).

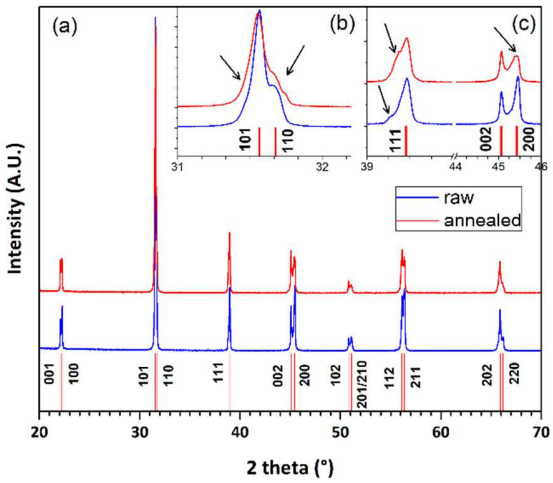

Figure 9. Patterns of as-grown and annealed BCTZ6 crushed single crystals. (a) Whole XRD pattern. (b) and (c) Details for selected peaks. The Miller indices are for the tetragonal phase. The arrows indicate the anomalies compared with the « pure » tetragonal phase.

Since the chemical analysis suggested the occurrence of two different compositions, we therefore considered the possibility of two simultaneous perovskite structures. Indeed, for the BCTZ compounds, Keeble *et al.*[5] evidenced that a change of composition around the phase convergence region induces a symmetry change: Tetragonal P4mm → Orthorhombic Amm2 → rhombohedral R3m[5]. Thus, we considered the following possibilities: P4mm + P4mm, P4mm + R3m, P4mm + Amm2. The best results were obtained for the last combination.

Therefore, Rietveld refinement was undertaken using the atomic positions and isotropic displacement parameters of the P4mm and Amm2 phases of $BaTiO_3$. Indeed, this combination explains well the splitting of the $(111)_{pc}$ peak, the intensity ratio of the $(00l)_{tetra}$ / $(h00)_{tetra}$ peaks and the distortion of the $(101)_{tetra}$ / $(110)_{tetra}$ peaks. Unfortunately, attempts to refine simultaneously the A-site and B-site contents were unsuccessful. Therefore, last refinements were performed using the chemical compositions estimated from the EPMA results: $(Ba_{0.884}Ca_{0.116})(Ti_{0.977}Zr_{0.023})O_3$ for the tetragonal phase and $(Ba_{0.922}Ca_{0.078})(Ti_{0.867}Zr_{0.133})O_3$ for the orthorhombic one. The results are represented in Figure 10 and the parameters from the Rietveld refinement are reported in Table 2. This two-phase refinement clearly explains: (i) the splitting of the $(00l)_{pc}$ peaks and the enlargement of the $(00l)_{tetra}$ peaks, (ii) the enlargement of the $(101)_{tetra}$ peak for low angles side and (iii) the observed splitting of the $(111)_{pc}$ peak. We can conclude that the Rietveld refinements clearly corroborate the presence of two phases with perovskite structures.

Quality of fit					
Rp		WRp		GOF	
7.34 %		9.91 %		1.88	
Relative phase amounts in mass : 62.3 / 37.7					
Tetragonal phase (P4mm)					
a (Å)		c (Å)		c /a	
3.9921		4.0215		1.007	
	x	y	z	Occupancy (%)	Biso
A-site (Ba/Ca)	0	0	0	88.4 / 11.6	0.10
B-site (Ti/Zr)	0.5	0.5	0.4876	97.7 / 2.3	0.10
O 1	0.5	0.5	0.0237	100	0.10
O 2	0.5	0	0.5163	100	0.10
Quality of fit					
R(obs)				WR(obs)	
4.48 %				5.28 %	
Orthorhombic phase (Amm2)					
a (Å)		b (Å)		c (Å)	
4.011		5.6850 (= 4.0199 x √2)		5.6744 (= 4.0124 x √2)	
	x	y	z	Occupancy (%)	Biso
A-site (Ba/Ca)	0	0	0	92.2 / 7.8	0.10
B-site (Ti/Zr)	0.5	0	0.517	86.7 / 13.3	0.10
O 3	0	0	0.4890	100	0.10
O 4	0.5	0.256	0.234	100	0.10
Quality of fit					
R(obs)				WR(obs)	
3.80 %				4.82 %	

Table 2. Results of the Rietveld refinements for BCTZ6.

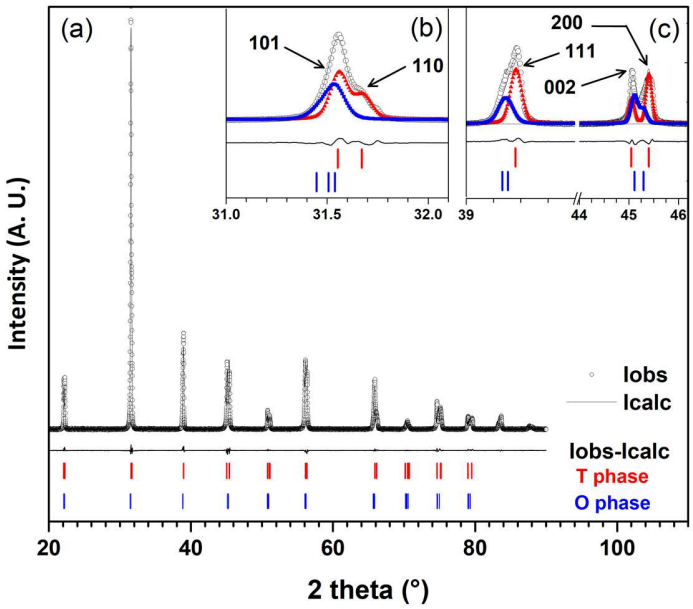

Figure 10. Results of the Rietveld refinement for annealed BCTZ6 crushed single crystal, (a) 20-90° pattern refinement fit using tetragonal P4mm + orthorhombic Amm2 structures, (b) and (c) details for selected peaks (the Miller indices are for tetragonal phase).

3.4 Dielectric and electromechanical characterization

Selected polycrystals displayed a rough textured structure with random orientation within 5° to 10° of mismatch in between each grain orientation composing the samples. Single crystals with $(001)_{pc}$ and $(110)_{pc}$ direction were oriented and cut within 1° of accuracy. Dielectric and piezoelectric characterization have been performed on samples originated from BCTZ4 to BCTZ6 polycrystalline boules and from BCTZ6 and BCTZ7 single crystals with various compositions (Table 3).

Attempt	Type	Electrical behaviour	Chemical formula	T_{max} or T_c (°C)	ε'	k_t or k_p (%)	d_{33} ($pC.N^{-1}$)	Tan δ (%)	Reference
BCTZ 4	mm-sized polycrystal	Relaxor	$(Ba_{0.874}Ca_{0.126})(Ti_{0.794}Zr_{0.206})O_3$	-90	3500	-	-	<1	This work
BCTZ 4	mm-sized polycrystal	Ferroelectric	$(Ba_{0.816}Ca_{0.184})(Ti_{0.928}Zr_{0.072})O_3$	55	2444	58	457	<1	This work
BCTZ 4	mm-sized polycrystal	Ferroelectric	$(Ba_{0.794}Ca_{0.206})(Ti_{0.911}Zr_{0.089})O_3$	57	2466	57	496	<1	This work
BCTZ 4	mm-sized polycrystal	Ferroelectric	$(Ba_{0.823}Ca_{0.177})(Ti_{0.865}Zr_{0.135})O_3$	50	5450	X	125	1,52	This work
BCTZ 5	mm-sized polycrystal	Ferroelectric	$(Ba_{0.784}Ca_{0.216})(Ti_{0.966}Zr_{0.034})O_3$	90	1009	44,7	190	<1	This work
BCTZ 6	mm-sized polycrystal	Ferroelectric	$(Ba_{0.914}Ca_{0.086})(Ti_{0.901}Zr_{0.099})O_3$	105	3912	48	368	<1	This work
BCTZ 6	$(001)_{pc}$ single crystal n°1	Ferroelectric	$(Ba_{0.905}Ca_{0.095})(Ti_{0.943}Zr_{0.057})O_3$	108	1092	37,6	350	1,78	This work
BCTZ 6	$(001)_{pc}$ single crystal n°2	Ferroelectric	$(Ba_{0.905}Ca_{0.095})(Ti_{0.943}Zr_{0.057})O_3$	106	1541	24,5	345	1,89	This work
BCTZ 6	$(001)_{pc}$ single crystal n°3	Ferroelectric	$(Ba_{0.905}Ca_{0.095})(Ti_{0.943}Zr_{0.057})O_3$	106	987	45,5	340	1,71	This work
BCTZ 6	$(110)_{pc}$ single crystal n°4	Ferroelectric	$(Ba_{0.905}Ca_{0.095})(Ti_{0.943}Zr_{0.057})O_3$	106	1828	46,8	234	<1	This work
BCTZ 7	$(001)_{pc}$ single crystal	Ferroelectric	$(Ba_{0.943}Ca_{0.057})(Ti_{0.966}Zr_{0.034})O_3$	111	1383	45,44	206	<1	This work
BCTZ 3	$(001)_{pc}$ single crystal	Ferroelectric	$(Ba_{0.838}Ca_{0.162})(Ti_{0.854}Zr_{0.146})O_3$	64	-	0,18	93	-	[12]
-	Ceramic	Ferroelectric	$(Ba_{0.92}Ca_{0.08})(Ti_{0.95}Zr_{0.05})O_3$	110	-	48,6	360	-	[37]
-	Ceramic	Ferroelectric	$(Ba_{0.94}Ca_{0.06})(Ti_{0.895}Zr_{0.105})O_3$	92.4	-	-	430	-	[36]
-	Ceramic	Ferroelectric	$(Ba_{0.90}Ca_{0.10})(Ti_{0.90}Zr_{0.10})O_3$	82.4	-	52,2	429	-	[35]
-	Ceramic	Ferroelectric	$(Ba_{0.875}Ca_{0.125})(Ti_{0.90}Zr_{0.10})O_3$	84.6	-	54,1	459	-	[35]
-	Ceramic	Ferroelectric	$(Ba_{0.825}Ca_{0.175})(Ti_{0.90}Zr_{0.10})O_3$	80.5	-	54,2	511	-	[35]
-	Ceramic	Ferroelectric	$(Ba_{0.85}Ca_{0.15})(Ti_{0.88}Zr_{0.12})O_3$	68.9	-	51,5	506	-	[35]
-	$(001)_{pc}$ single crystal	Ferroelectric	$(Ba_{0.798}Ca_{0.202})(Ti_{0.994}Zr_{0.006})O_3$	125	-	-	232	-	[40]
-	$(001)_{pc}$ single crystal	Ferroelectric	$(Ba_{0.982}Ca_{0.018})(Ti_{0.999}Zr_{0.001})O_3$	120	-	-	200	-	[39]
-	Ceramic	Ferroelectric	$(Ba_{0.85}Ca_{0.15})(Ti_{0.90}Zr_{0.10})O_3$	93	-	-	620	-	[10]
-	Ceramic	Ferroelectric	$(Ba_{0.92}Ca_{0.08})(Ti_{0.92}Sn_{0.08})O_3$	RT	-	60	550	-	[42]
-	$(001)_{pc}$ single crystal	Ferroelectric	$(K_{0.45}Na_{0.55})_{0.96}Li_{0.04}NbO_3$	432	-	-	689	-	[43]
-	$(001)_{pc}$ single crystal	Ferroelectric	$(K_{0.287}Na_{0.691}Li_{0.022})(Nb_{0.870}Ta_{0.063}Sb_{0.067})O_3$	279	-	-	732	-	[9]
-	Ceramic	Ferroelectric	PZT-5H	190	3400	75	590	2	[1]
-	Ceramic	Ferroelectric	PZT-5A (soft)	365	1700	71	375	2	[1]
-	Ceramic	Ferroelectric	PZT-8 (hard)	300	1000	64	225	0,4	[1]

Table 3. Dielectric and piezoelectric functional data measured at room temperature (RT) and electrical features of lead-based and lead-free reference materials.

On the one hand, as a global tendency, electrical behaviors of the samples are in good agreement with literature about ceramics with close compositions[32–37] and are of the same order of magnitude than standard PZT ceramics[1] (Table 3). Decreasing Curie temperatures are observed with increasing Zr content until samples become relaxor because the long range ferroelectric order is disrupted at microscopic level with increasing Zr concentration[38]. All the samples show low electrical losses (tan δ). BCTZ4 polycrystal displayed a high d_{33}= 496$pC.N^{-1}$ similar to that of ceramics with close compositions[10,32]. Although piezoelectric coefficients d_{33} are higher than those previously reported in lead-free BCTZ single crystals[13,39,40], they remain below the predicted ones[10] and those of other lead-free systems[9,41–43]. This feature is mainly due to the fact that BCTZ polycrystals exhibit averaged properties compared to those of single crystals. Besides, owing to

the difficulty to compare lead-free piezoelectric systems with each other, because different polarization mechanisms occur[5,10,44,45], we assume that the domain configuration and size play an important role on the piezoelectric response as previously reported[40,46]. In addition, as suggested by Imura *et al.* [47] for BCT system, $CaTiO_3$-like octahedral rotation may be constructed in the BCZT cell around the Ca atoms and may be the origin of the weak spontaneous polarization in BCTZ crystals and thus, of a weaker piezoelectric response than expected. Finally, minute composition changes[4] as well as chemical fluctuations may induce a sharp decreasing of the piezoelectric performance. BCTZ crystals of the present work, in particular for BCTZ4 mm-sized polycrystals (see Table 3) that shows the best d_{33} and the closest composition to that of Liu *et al.*[10] exhibit sufficient contents differences for lowering substantially the piezoelectric response that lie thus below the predicted value of 1500 $pC.N^{-1}$.

On the other hand, several BCTZ6 $(001)_{pc}$ oriented crystals with same average composition and one $(110)_{pc}$ oriented crystal display T_c near 106°C-108°C with d_{33} up to 350 $pC.N^{-1}$ and a thickness coupling constant around k_t=45%. Discrepancy of measured k_{33} is assumed to be induced by small dimension of the plate and chemical contents variation in the whole sample volume due to the effective segregation of elements as well as to the spinodal decomposition.

Whether the samples were poled up to 1$kV.mm^{-1}$ or not (Figure 11a and b), dielectric measurements performed on as-grown and annealed BCTZ6 single crystals show the same behaviour with a broadening of the low temperature Orthorhombic-Tetragonal (O-T) dielectric anomaly in the range [-40°C; 20°C] without change of the Tetragonal-Cubic (T-C) temperature. This latter anomaly exhibits symmetric transition whose the full width at half maximum tends to slightly diminish after annealing. As previously referenced, Ca cations in BCTZ system may behave as in $(Ba_{1-x}Ca_x)TiO_3$ (BCT) system because of the same investigated Ca content range. Ca

content up to 20% in BCT solid solution keeps the Curie temperature unaffected[48] compared to that of pure $BaTiO_3$ whereas the other phase transition temperatures are substantially lowered with Ca content [49–51]. Spinodal phase separation induced the broadening of the O-T anomaly which is actually composed of the two transition anomalies close to each other corresponding to the signature of each phase with different Ca content. Curie temperature at T-C phase transition is not impacted because of the same average Zr composition in the crystal sample. As suggested by previous works on relaxor-ferroelectric transition in lead-based materials[52,53], the sharpening of the T-C anomaly after annealing is assumed to be caused by the lowering of the spatial disorder of cations within the BCTZ perovskite matrix.

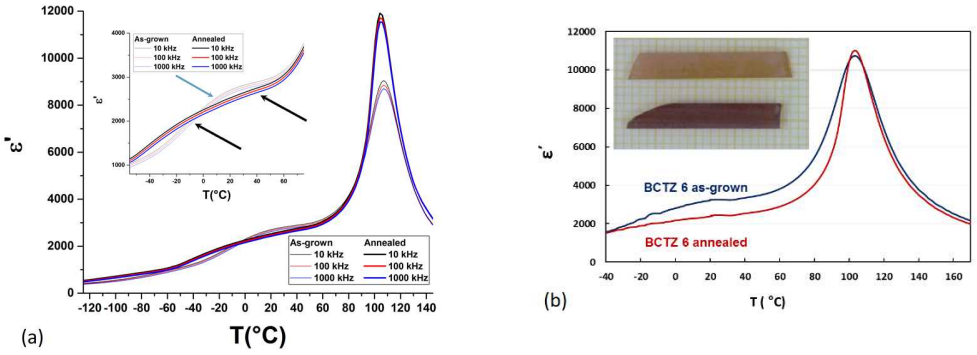

Figure 11. Relative permittivity as a function of temperature and frequencies for as-grown and annealed $(001)_{pc}$ (a) BCTZ6 unpoled sample and (b) poled sample (f= 1 kHz). Measurement has been performed during cooling down. Arrows in (a) indicate O-T anomalies. Insert: top: as-grown BCTZ6 single crystal; bottom: annealed BCTZ6 single crystal.

Conclusion

Crystal growth attempts in the $BaTiO_3$-$CaTiO_3$-$BaZrO_3$ pseudo-ternary system by Top Seeded Solution Growth are reported. Centimeter sized single crystals were obtained. Numerous samples

with various compositions have been extracted and shaped in order to perform suitable chemical and physical analysis. EPMA analysis of BCTZ crystals revealed that the as-grown crystals are enriched with zirconium and barium compared to the initial content because of the difference of elemental effective partition coefficients in the crystal.

Close to the composition range of interest for piezoelectric applications, we observed that a spinodal decomposition occurred during the growth leading thus to the emergence of two solid solutions of close compositions with tetragonal P4mm and orthorhombic Amm2 space groups. Although variations and periodical fluctuations of Ca and Zr induce lower piezoelectric values than those expected, this result could be considered as a first step toward further optimization of the piezoelectric properties of BCTZ single crystals. Fluctuating concentrations could induce a higher polarization flexibility and thus a better piezoelectric response. For instance, an excellent piezoelectric constants d_{33} up to 496 $pC.N^{-1}$ with k_t= 58% by the Berlincourt method was obtained in $(Ba_{0.794}Ca_{0.206})(Ti_{0.911}Zr_{0.089})O_3$ polycrystalline BCTZ with mm-sized grains.

Since dielectric losses are low, further attempts at growing BCTZ by decreasing the Zr and Ca contents which are likely to be detrimental to the Curie temperature will enable to reach efficient piezoelectric constant with a high Curie temperature making BCTZ a promising competitor to lead-based materials.

Acknowledgement

The authors acknowledge ANR program through HECATE project (n°14-CE07-0028) and the Innovative Training Networks (ITN) - Marie Skłodowska-Curie Actions - European Joint Doctorate in Functionnal Materials Research (EJDFunMat) project (n°641640) for financial and technical supports.

References

(1) Shrout, T. R.; Zhang, S. J. Lead-Free Piezoelectric Ceramics: Alternatives for PZT? *J. Electroceramics* **2007**, *19*, 111–124.

(2) Zhang, S.; Xia, R.; Shrout, T. R. Lead-Free Piezoelectric Ceramics vs. PZT? *J. Electroceramics* **2007**, *19*, 251–257.

(3) Rödel, J.; Jo, W.; Seifert, K. T. P.; Anton, E. M.; Granzow, T.; Damjanovic, D. Perspective on the Development of Lead-Free Piezoceramics. *J. Am. Ceram. Soc.* **2009**, *92*, 1153–1177.

(4) Prakasam, M.; Veber, P.; Viraphong, O.; Etienne, L.; Lahaye, M.; Pechev, S.; Lebraud, E.; Shimamura, K.; Maglione, M. Growth and Characterizations of Lead-Free Ferroelectric KNN-Based Crystals. *Comptes Rendus Phys.* **2013**, *14*, 133–140.

(5) Keeble, D. S.; Benabdallah, F.; Thomas, P. A.; Maglione, M.; Kreisel, J. Revised Structural Phase Diagram of $(Ba_{0.7}Ca_{0.3}TiO_3)$-$(BaZr_{0.2}Ti_{0.8}O_3)$. *Appl. Phys. Lett.* **2013**, *102*, 092903.

(6) Acosta, M.; Novak, N.; Rojas, V.; Patel, S.; Vaish, R.; Koruza, J.; Rossetti, G. A.; Rödel, J. $BaTiO_3$-Based Piezoelectrics: Fundamentals, Current Status, and Perspectives. *Appl. Phys. Rev.* **2017**, *4*, 041305.

(7) Saito, Y.; Takao, H.; Tani, T.; Nonoyama, T.; Takatori, K.; Homma, T.; Nagaya, T.; Nakamura, M. Lead-Free Piezoceramics. *Nature* **2004**, *432*, 84–87.

(8) Liu, H.; Koruza, J.; Veber, P.; Rytz, D.; Maglione, M.; Rödel, J. Orientation-Dependent Electromechanical Properties of Mn-Doped $(Li,Na,K)(Nb,Ta)O_3$ Single Crystals. *Appl. Phys. Lett.* **2016**, *109*, 152902.

(9) Liu, H.; Veber, P.; Rödel, J.; Rytz, D.; Fabritchnyi, P. B.; Afanasov, M. I.; Patterson, E. A.; Frömling, T.; Maglione, M.; Koruza, J. High-Performance Piezoelectric

(K,Na,Li)(Nb,Ta,Sb)O_3 Single Crystals by Oxygen Annealing. *Acta Mater.* **2018**, *148*, 499–507.

(10) Liu, W.; Ren, X. Large Piezoelectric Effect in Pb-Free Ceramics. *Phys. Rev. Lett.* **2009**, *103*, 257602.

(11) Nahas, Y.; Akbarzadeh, A.; Prokhorenko, S.; Prosandeev, S.; Walter, R.; Kornev, I.; Íñiguez, J.; Bellaiche, L. Microscopic Origins of the Large Piezoelectricity of Lead-free (Ba,Ca)(Zr,Ti)O_3. *Nat. Commun.* **2017**, *8*, 1.

(12) Benabdallah, F.; Veber, P.; Prakasam, M.; Viraphong, O.; Shimamura, K.; Maglione, M. Continuous Cross-over from Ferroelectric to Relaxor State and Piezoelectric Properties of $BaTiO_3$-$BaZrO_3$-$CaTiO_3$ Single Crystals. *J. Appl. Phys.* **2014**, *115*, 144102.

(13) Veber, P.; Benabdallah, F.; Liu, H.; Buse, G.; Josse, M.; Maglione, M. Growth and Characterization of Lead-Free Piezoelectric Single Crystals. *Materials (Basel).* **2015**, *8*, 7962–7978.

(14) ANSI/IEEE Std 176-1987. An American National Standard IEEE-Standard on Piezoelectricity. The Institute of Electrical and Electronics Engineers 1988.

(15) Petříček, V.; Dušek, M.; Palatinus, L. Crystallographic Computing System JANA2006: General Features. *Zeitschrift für Krist.* **2014**, *229*, 345–352.

(16) $BaTiO_3$ Crystal Structure, Lattice Parameters. In *Ternary Compounds, Organic Semiconductors*; Madelung, O., Rössler, U., Schulz, M., Eds.; Springer Berlin Heidelberg: Berlin, Heidelberg, 2000; pp 1–6.

(17) Glaister, R. M.; Kay, H. F. An Investigation of the Cubic-Hexagonal Transition in Barium Titanate. *Proc. Phys. Soc.* **1960**, *76*, 763–771.

(18) Basmajian, J. A.; Devries, R. C. Phase Equilibria in the System $BaTiO_3$-$SrTiO_3$. *J. Am. Ceram. Soc.* **1957**, *40*, 373–376.

(19) Ceh, M.; Kolar, D.; Golic, L. The Phase Diagram of $CaTiO_3$-$SrTiO_3$. *J. Solid State Chem.* **1987**, *68*, 68–72.

(20) Redfern, S. A. T. High-Temperature Structural Phase Transitions in Perovskite (CaTiO3). *J. Phys. Condens. Matter* **1996**, *8*, 8267–8275.

(21) Guennou, M.; Bouvier, P.; Krikler, B.; Kreisel, J.; Haumont, R.; Garbarino, G. High-Pressure Investigation of $CaTiO_3$ up to 60 GPa Using x-Ray Diffraction and Raman Spectroscopy. *Phys. Rev. B - Condens. Matter Mater. Phys.* **2010**, *82*, 1–10.

(22) Jiang, Y. J.; Guo, R. Y.; Bhalla, a S. Growth and Properties of $CaTiO_3$ Single Crystal Fibers. *J. Electroceramics* **1998**, *2*, 199–203.

(23) Yamashita, Y.; Ichinose, N. Can Relaxor Piezoelectric Materials Outperform PZT?(Review). In *Applications of Ferroelectrics, 1996. ISAF '96., Proceedings of the Tenth IEEE International Symposium on*; 1996; pp 71–78.

(24) Devries, R. C.; Roy, R. Phase Equilibria in the System $BaTiO_3$-$CaTiO_3$. *J. Am. Soc.* **1955**, *38*, 158–171.

(25) Halvorson, J. J.; Wimber, R. T. Thermal Expansion of Iridium at High Temperatures. *J. Appl. Crystallogr.* **1972**, *43*, 2519.

(26) He, Y. Heat Capacity , Thermal Conductivity , and Thermal Expansion of Barium Titanate-Based Ceramics. *Thermochim. Acta* **2004**, *419*, 135–141.

(27) Schwabe, D.; Uecker, R.; Bernhagen, M.; Galazka, Z. An Analysis of and a Model for Spiral Growth of Czochralski-Grown Oxide Crystals with High Melting Point. *J. Cryst. Growth*

2011, *335*, 138–147.

(28) Guguschev, C.; Kok, D. J.; Galazka, Z.; Klimm, D.; Uecker, R.; Bertram, R.; Naumann, M.; Juda, U.; Kwasniewski, A.; Bickermann, M. Influence of Oxygen Partial Pressure on $SrTiO_3$ Bulk Crystal Growth from Non-Stoichiometric Melts. *CrystEngComm* **2015**, *17*, 3224–3234.

(29) Jackson, K. A. *Kinetics Processes: Crystal Growth, Diffusion, and Phase Transitions in Materials*; WILEY-VCH Verlag GmbH & Co. KGaA, Weinheim, 2004.

(30) Levin, I.; Amos, T. G.; Bell, S. M.; Farber, L.; Vanderah, T. A.; Roth, R. S.; Toby, B. H. Phase Equilibria, Crystal Structures, and Dielectric Anomaly in the $BaZrO_3$-$CaZrO_3$ System. *J. Solid State Chem.* **2003**, *175*, 170–181.

(31) Benabdallah, F.; Simon, A.; Khemakhem, H.; Elissalde, C.; Maglione, M. Linking Large Piezoelectric Coefficients to Highly Flexible Polarization of Lead Free $BaTiO_3$-$CaTiO_3$-$BaZrO_3$ Ceramics. *J. Appl. Phys.* **2011**, *109*, 124116.

(32) Ravez, J.; Broustera, C.; Simon, A. Lead-Free Ferroelectric Relaxor Ceramics in the $BaTiO_3$-$BaZrO_3$-$CaTiO_3$ System. *J. Mater. Chem.* **1999**, *9*, 1609–1613.

(33) Simon, A.; Ravez, J.; Maglione, M. Relaxor Properties of $Ba_{0.9}Bi_{0.067}(Ti_{1-x}Zr_x)O_3$ Ceramics. *Solid State Sci.* **2005**, *7*, 925–930.

(34) Zeng, Y.; Zheng, Y.; Tu, X.; Lu, Z.; Shi, E. Growth and Characterization of Lead-Free $Ba_{(1-x)}Ca_xTi_{(1-y)}Zr_yO_3$ Single Crystal. *J. Cryst. Growth* **2012**, *343*, 17–20.

(35) Tian, Y.; Wei, L.; Chao, X.; Liu, Z.; Yang, Z. Phase Transition Behavior and Large Piezoelectricity Near the Morphotropic Phase Boundary of Lead-Free $(Ba_{0.85}Ca_{0.15})(Zr_{0.1}Ti_{0.9})O_3$ Ceramics. *J. Am. Ceram. Soc.* **2013**, *96*, 496–502.

(36) Bao, H.; Zhou, C.; Xue, D.; Gao, J.; Ren, X. A Modified Lead-Free Piezoelectric BZT– x BCT System with Higher T C. *J. Phys. D. Appl. Phys.* **2010**, *43*, 465401.

(37) Li, W.; Xu, Z.; Chu, R.; Fu, P.; Zang, G. Piezoelectric and Dielectric Properties of $(Ba_{1-x}Ca_x)(Ti_{0.95}Zr_{0.05})O_3$ Lead-Free Ceramics. *J. Am. Ceram. Soc.* **2010**, *93*, 2942–2944.

(38) Buscaglia, V.; Tripathi, S.; Petkov, V.; Dapiaggi, M.; Deluca, M.; Gajović, A.; Ren, Y. Average and Local Atomic-Scale Structure in $BaZr_xTi_{1-x}O_3$ (x = 0.10, 0.20, 0.40) Ceramics by High-Energy x-Ray Diffraction and Raman Spectroscopy. *J. Phys. Condens. Matter* **2014**, *26*, 065901.

(39) Sun, Y.; Liu, D.; Li, Q.; Shim, J.; He, W.; Fang, H.; Yan, Q. Piezoelectric Property of a Tetragonal (Ba,Ca)(Zr,Ti)O_3 Single Crystal and Its Fine-Domain Structure. *ACS Appl. Mater. Interfaces* **2018**, *10*, 12847−12853.

(40) Liu, D.; Shim, J.; Sun, Y.; Li, Q.; Yan, Q. Growth of Ca, Zr Co-Doped $BaTiO_3$ Lead-Free Ferroelectric Single Crystal and Its Room-Temperature Piezoelectricity. *AIP Adv.* **2017**, *7*, 095311.

(41) Zhu, L.-F.; Zhang, B.-P.; Zhao, L.; Li, S.; Zhou, Y.; Shi, X.-C.; Wang, N. Large Piezoelectric Effect of (Ba,Ca)TiO_3–xBa(Sn,Ti)O_3 Lead-Free Ceramics. *J. Eur. Ceram. Soc.* **2016**, *36*, 1017–1024.

(42) Yang, Y.; Zhou, Y.; Ren, J.; Zheng, Q.; Lam, K. H.; Lin, D. Phase Coexistence and Large Piezoelectricity in $BaTiO_3$-$CaSnO_3$ Lead-Free Ceramics. *J. Am. Ceram. Soc.* **2018**, *101*, 2594–2605.

(43) Yang, J.; Zhang, F.; Yang, Q.; Liu, Z.; Li, Y.; Liu, Y.; Zhang, Q. Large Piezoelectric Properties in KNN-Based Lead-Free Single Crystals Grown by a Seed-Free Solid-State

Crystal Growth Method. *Appl. Phys. Lett.* **2016**, *108*, 182904.

(44) Damjanovic, D. A Morphotropic Phase Boundary System Based on Polarization Rotation and Polarization Extension. *Appl. Phys. Lett.* **2010**, *97*, 062906.

(45) Tian, H.; Meng, X.; Hu, C.; Tan, P.; Cao, X.; Shi, G.; Zhou, Z.; Zhang, R. Origin of Giant Piezoelectric Effect in Lead-Free $K_{1-x}Na_xTa_{1-y}Nb_yO_3$ Single Crystals. *Sci. Rep.* **2016**, *6*, 25637.

(46) Liu, H.; Veber, P.; Zintler, A.; Molina-Luna, L.; Rytz, D.; Maglione, M.; Koruza, J. Temperature-Dependent Evolution of Crystallographic and Domain Structures in (K,Na,Li)(Ta,Nb)O_3 Piezoelectric Single Crystals. *IEEE Trans. Ultrason. Ferroelectr. Freq. Control,* **2018,** *65*, 1508-1516.

(47) Imura, R.; Kitanaka, Y.; Oguchi, T.; Noguchi, Y.; Miyayama, M. Polarization Properties and Crystal Structures of Ferroelectric (Ba,Ca)TiO_3 Single Crystals. *J. Adv. Dielectr.* **2014**, *4*, 1450003.

(48) Levin, I.; Krayzman, V.; Woicik, J. C. Local-Structure Origins of the Sustained Curie Temperature in (Ba,Ca)TiO_3 Ferroelectrics. *Appl. Phys. Lett.* **2013**, *102*, 1–6.

(49) Fu, D.; Itoh, M.; Koshihara, S. Crystal Growth and Piezoelectricity of $BaTiO_3$-$CaTiO_3$ Solid Solution. *Appl. Phys. Lett.* **2008**, *93*, 012904.

(50) Fu, D.; Itoh, M.; Koshihara, S.; Kosugi, T.; Tsuneyuki, S. Anomalous Phase Diagram of Ferroelectric (Ba,Ca)TiO_3 Single Crystals with Giant Electromechanical Response. *Phys. Rev. Lett.* **2008**, *100*, 227601.

(51) Mitsui, T.; Westphal, W. B. Dielectric and X-Rays Studies of $Ca_xBa_{1-x}TiO_3$ and $Ca_xSr_{1-x}TiO_3$. *Phys. Rev.* **1961**, *124*, 1354–1359.

(52) Bidault, O.; Perrin, C.; Caranoni, C.; Menguy, N. Chemical Order Influence on the Phase Transition in the Relaxor $Pb(Sc_{1/2}Nb_{1/2})O_3$. *J. Appl. Phys.* **2001**, *90*, 4115–4121.

(53) Chu, F.; Setter, N.; Tagantsev, A. K. The Spontaneous Relaxor-Ferroelectric Transition of $Pb(Sc_{0.5}Ta_{0.5})O_3$. *J. Appl. Phys.* **1993**, *74*, 5129–5134.